https://doi.org/10.26599/FRICT.2026.9441317

Research Article

Multilevel-structured phase-responsive solid–liquid composite lubricating coating and its tribological and anti-corrosion performance

Junhao Sang, Yunlong Li, Xinyuan Ji, Yongling Wu*, Mingming Liu*, Hongyu Zheng*

Centre for Advanced Laser Manufacturing (CALM), School of Mechanical Engineering, Shandong University of Technology, Zibo 255000, China

*Corresponding authors: ylwu06@sdut.edu.cn, mmliu_122@hotmail.com, zhenghongyu@sdut.edu.cn

Received: May 9, 2026; Revised: July 10, 2026; Accepted: September 10, 2026

ABSTRACT

Laser-induced graphene (LIG) has attracted widespread attention owing to its excellent solid-lubricating property, chemical stability, and designable surface structure, and has shown broad application prospects in fields such as friction reduction and corrosion protection. However, its limited structural stability and lubricant-storage capability restrict its practical application. In this work, a multifunctional composite lubricating surface integrating LIG, epoxy resin, laser surface texturing, and phase-change paraffin wax (PW@LST@E-LIG) was developed. The LIG structure was firstly optimized by tuning the laser power, followed by epoxy resin infiltration to enhance structural stability. Subsequently, laser-textured micropore arrays were introduced and combined with phase-change paraffin wax to establish a thermally responsive lubrication system, thereby achieving the synergistic enhancement of tribological and anti-corrosion performance. Compared with the original LIG, the optimized sample exhibited a reduction in coefficient of friction (COF) of 45–55% (approximately 0.09) and the wear depth decreased by approximately 90% under the same load. Anti-corrosion performance tests showed that the interfacial charge-transfer resistance increased to 10^5 Ω cm^2, while the corrosion current density decreased to 10^{-7} A·cm^{-2}. The corrosion current density decreased by more than two orders of magnitude compared with that of the substrate, resulting in an inhibition efficiency of 99.54%. Through the coupling of structural design and phase-change materials, this study achieved the synergistic enhancement of wear resistance, lubrication, lubricant-storage capability, and anti-corrosion performance, providing a new strategy for the design of

multifunctional surfaces for diverse service conditions.

Keywords: Laser-induced graphene (LIG); Laser surface texturing; Micropore array; Phase-change paraffin Wax; Adaptive tribological performance; Anti-corrosion performance.

1 Introduction

Friction, wear, and corrosion are key factors limiting the service performance of engineering materials under complex operating conditions. In marine, chemical, and manufacturing environments, these degradation processes generally do not occur independently, but rather interact with each other to accelerate surface damage and performance deterioration. In particular, under chloride-containing media, cyclic loading, and boundary lubrication conditions, friction-induced damage of the surface layer facilitates the penetration of corrosive species, while corrosion products and interfacial degradation further aggravate the tribological behavior. Therefore, the development of multifunctional surface systems with integrated friction-reducing, anti-wear, and anti-corrosion performance has become an important research topic in the fields of surface engineering and tribology[1-5].

Graphene and its derivatives have been widely regarded as highly promising materials for both friction-reducing performance and surface protection owing to their layered structure, low interlayer shear strength, and excellent chemical stability and barrier properties[6-8]. Among them, laser-induced graphene (LIG) can be directly

fabricated through the one-step in situ conversion of precursors such as polyimide by laser irradiation, featuring a simple process, good patterning capability, low cost, and a three-dimensional porous framework[9-12]. Xue et al. investigated the tribological behavior of laser-induced graphene (LIG) films on silicon substrates with different roughness levels, demonstrating that the films exhibited excellent tribological adaptability on both mirror-polished and rough substrates[13]. Wang et al. constructed a multifunctional LIG composite coating by combining laser-induced graphene with post-modification using a silica sol binder, endowing the surface with both electro-/photothermal deicing capability and superhydrophobic anti-icing performance[14]. In addition to its tribological advantages, graphene-based coatings have also attracted extensive attention in corrosion protection because they can prolong the diffusion path of corrosive species and increase the interfacial charge-transfer resistance [15-19]. Batista et al. fabricated multilayer flexible GO/rGO composite coatings on NiTi alloy surfaces by a dip-coating method, and the results showed that graphene composite coatings could significantly enhance the anti-corrosion performance of the alloy[20]. Hashemi et al. fabricated an anticorrosive LIG protective layer by tuning the laser power and incorporating alkyd resin encapsulation, which exhibited excellent protective capability for metallic surfaces[21]. The above-mentioned studies demonstrate that LIG and graphene surfaces possess considerable potential for simultaneously improving tribological and anti-corrosion performance. However, bare LIG surfaces still suffer from fragile pore walls, local structural collapse, and insufficient long-term service stability. Particularly under relatively high loads and

repeated shear, the porous framework is prone to compaction, delamination, and even structural instability, which weakens its self-lubricating effect and undermines the integrity of the protective barrier. Moreover, after encapsulation with epoxy or similar materials, although the surface integrity and barrier capability are improved, the epoxy layer bears most of the applied load, thereby weakening the intrinsic self-lubricating effect of graphene. Therefore, further interfacial design is required to simultaneously enhance the tribological performance, lubricant retention, and durability of graphene-based protective surfaces.

Laser surface texturing provides an effective route to address this issue. By constructing regular micro-pits, micro-grooves, and related surface features, the real contact area can be effectively reduced, while wear debris and lubricants can be retained and the contact stress distribution can be improved, thereby enhancing the load-carrying and lubrication capacities of tribological interfaces[22-28]. Cao et al. reported that the synergistic effect, achieved by constructing Ag coatings with different micro-dimple textures on copper surfaces and combining them with multilayer graphene grease, could significantly enhance the friction-reducing and anti-wear performance, as well as the electrical contact performance, of the Ag coatings[29]. Li et al. demonstrated that, by fabricating dimple arrays with different geometric parameters on GCr15 steel surfaces and combining them with graphene/5CB suspension lubrication, the friction-reducing and anti-wear performance under starved lubrication conditions could be significantly improved[30]. The combination of graphene-based lubricants with laser surface texturing has been demonstrated to effectively improve tribological performance by

enhancing lubricant storage, debris trapping, and contact-state regulation.

However, relying solely on static micro/nanostructures or conventional solid fillings is still insufficient to meet the requirement for long-term stable lubrication under complex service conditions; once the interfacial structure is disrupted, the COF and wear rate tend to increase rapidly. In contrast, phase-change lubricants, and self-healing protective layers provide new approaches to address this issue[31-35]. Xue et al. developed lubricating nanocapsules based on the phase-transition behavior of deep eutectic solvents and incorporated them into an epoxy system, thereby enabling in situ real-time monitoring of tribological interface temperature while simultaneously enhancing the friction-reducing and anti-wear performance[36]. Song et al. constructed a skeleton based on LIG and incorporated a phase-change paraffin wax-based ferrofluid, thereby fabricating an intelligent surface with multiple responsiveness and anisotropic lubricating and friction-reducing properties[37]. This study demonstrates the potential of integrating LIG-based frameworks with phase-change lubricants to realize responsive interfacial lubrication. However, the surface load-bearing capacity of this system remains limited, and the lubricant-storage volume provided solely by the LIG skeleton is insufficient for sustained lubricant supply during long-term sliding. Based on the above analysis of the existing composite coatings, constructing a composite coating that simultaneously integrates structural reinforcement, solid lubrication, lubricant storage, thermally responsive replenishment, and corrosion protection remains a key challenge.

In this study, we proposed a multilevel-structured composite surface. First, LIG

was in situ generated on the PI surface by tuning the laser power to obtain a functional layer with an appropriate degree of graphitization and a porous framework. Epoxy resin infiltration was then performed to enhance structural stability. Subsequently, micropore arrays with different pore-area densities were constructed to regulate the balance between lubricant-storage space and load-bearing regions. Finally, phase-change paraffin was incorporated to enable dynamic lubricant replenishment driven by the solid-liquid transition. The effects of laser power, epoxy resin infiltration, micropore area density, and paraffin wax phase-transition behavior on the tribological and anti-corrosion performance of the surface were systematically investigated, and the corresponding synergistic mechanisms were discussed. This study is expected to provide a new strategy for the design of multifunctional self-lubricating protective surfaces for complex service conditions.

2 Experimental Section

2.1 Materials

42CrMo steel was purchased from Dongguan Gangyi Special Steel Co., Ltd. Polyimide (PI) solution was supplied by DuPont. Thermosetting epoxy resin (hereinafter referred to as epoxy) was purchased from Beijing Fucai Yigou Technology Co., Ltd. Phase-change paraffin waxes (hereinafter referred to as paraffin wax) with phase-transition temperatures of 20 °C, 40 °C, and 60 °C were obtained from Dongguan Shengbang Polymer Materials Co., Ltd. A CO_2 laser system was purchased from Shandong Leize Intelligent Technology Co., Ltd., while the picosecond laser system used in this study was provided by Wuhan Anyang Laser Technology Co., Ltd. All

chemicals used in this work were of analytical grade and were used without further purification. Deionized water was used throughout the entire experimental procedure.

2.2 Preparation of the composite coating

2.2.1 Preparation of the E-LIG coating

In this study, 42CrMo steel was selected as the substrate material and machined into block specimens with dimensions of 25 mm × 25 mm × 2 mm. Prior to LIG fabrication, the sample surfaces were sequentially polished with 500#, 1000#, and 1500# abrasive papers, followed by ultrasonic cleaning in anhydrous ethanol to remove surface contaminants. The cleaned samples were then dried in a vacuum oven to ensure a clean surface for subsequent treatment. As shown in Fig. 1(a), a polyimide (PI) layer was first spin-coated onto the surface of the 42CrMo steel substrate and then cured in an oven at 200 °C for 2 h to obtain the PI layer, the thickness of which was controlled within the range of 80 - 120 μm. Subsequently, as illustrated in Fig. 1(b), the PI layer was converted into a graphene layer using a 40 W CO_2 infrared laser system. The power range is 8 - 18 W, and the detailed laser parameters are listed in Table S1. The laser system allowed the scanning speed to be adjusted from 0 to 2000 mm s^{-1}, with a focal length of 28 cm. The thickness of the LIG layer was controlled at approximately 100 μm. The samples prepared under different laser powers were denoted as LIG8, LIG10, LIG12, LIG14, LIG16, and LIG18, respectively. The corresponding energy densities at different laser powers are summarized in Table S2.

The thermosetting epoxy consisted of bisphenol A epoxy and an amine curing agent, which were mixed at a mass ratio of 100:33 and ultrasonically stirred for 5 min.

The prepared mixture was then uniformly applied onto the as-fabricated LIG samples. Since the LIG possessed a porous three-dimensional structure, vacuum treatment was employed for 15 min after coating to ensure complete impregnation of the epoxy. During this process, the trapped gas within the pores was removed, and after releasing the vacuum, the epoxy was driven into the pores and sealed under atmospheric pressure. The coated samples were subsequently spin-coated for uniform distribution and cured in an oven at 60 °C for 1 h, followed by further curing at 120 °C for 2 h. In this way, the E-LIG samples were obtained (Fig. 1(c)). The coating thickness was approximately 200 μm, with about 100 μm extending above the original LIG surface to facilitate subsequent processing. The resulting samples were denoted as E-LIG8, E-LIG10, E-LIG12, E-LIG14, E-LIG16, and E-LIG18, respectively.

2.2.2 Preparation of the PW@LST@E-LIG coating

The coating surface was further laser-textured using a picosecond laser system, as shown in Fig. 1(d), and the detailed laser parameters are listed in Table S3. Considering the thickness of the epoxy layer above the LIG surface (approximately 100 μm), a pore diameter of 400 μm was selected to balance lubricant storage capacity and load-bearing capability. Under the above laser processing conditions, cylindrical micropores with a diameter of 400 μm and a depth of 100 μm were obtained. In general, the typical range of textured surface density is 5–40%[38, 39]. In the present work, to ensure sufficient lubricant-storage capacity, an intermediate value, a relatively high value, and an extreme value of surface density were selected. Accordingly, three textured surface densities, namely 20%, 40%, and 50%, were designed, and their corresponding

performance was analyzed in relation to the effective contact area. The theoretical lubricant-storage capacities of samples with different micropore densities are summarized in Table S4. The resulting samples were denoted as 20LST@E-LIG, 40LST@E-LIG, and 50LST@E-LIG, respectively.

The temperature was first raised above the melting point of the paraffin wax, after which the textured samples were immersed in the molten paraffin wax to ensure complete infiltration and full filling of the micropores. After vertical draining for 5 min, a lubricating surface capable of solid-liquid transition was successfully obtained, with the paraffin wax layer thickness being approximately 200 μm. To accommodate fluctuations in ambient temperature and climatic variations, paraffin waxes with different solid-liquid phase-transition temperatures (20 °C, 40 °C, and 60 °C) were introduced into the surface textures as lubricants. The resulting samples (Figs. 1(e) and 1(f)) were denoted as 20PW@LST@E-LIG, 40PW@LST@E-LIG, and 60PW@LST@E-LIG, respectively.

2.3 Tribological performance tests

Reciprocating sliding tests were carried out on a tribometer (TriboStudio TS20) with a stroke length of 5 mm, a frequency of 2-5 Hz, a normal load of 1-10 N, and a test duration of 0.5 h. A GCr15 bearing steel ball with a diameter of 5 mm was used as the counterpart. The temperature-responsive tribological tests were conducted using the temperature-control module integrated with the tribometer. The average heating rate was 5 °C·min^{-1}, and the temperature evolution was monitored in real time using an infrared thermal imaging camera. After completion of the tribological tests, the three-

dimensional surface topography was characterized using a laser scanning confocal microscope (KC-X1000) within a scanning area of 2000 μm × 2000 μm. Each tribological test was repeated three times under the same testing conditions using independent samples or fresh unworn regions. The average COF was calculated from the steady-state region after the running-in stage. The standard deviation was calculated using the sample standard deviation formula, and the error bars represent the standard deviations of the repeated tests.

2.4 Anti-corrosion performance tests

A conventional three-electrode electrochemical system was established on an IVIUM electrochemical workstation (the Netherlands) to evaluate the anti-corrosion performance of the coated samples. In this setup, a saturated calomel electrode (SCE) was used as the reference electrode, a platinum electrode served as the counter electrode, and the coated sample acted as the working electrode with an exposed area of 1 cm^2. During the measurements, the electrode system was first immersed in a 3.5 wt.% NaCl solution to record the open-circuit potential (OCP), after which the working electrode was stabilized at the OCP for 1800 s to ensure that a steady-state condition was reached. Potentiodynamic polarization tests were then conducted within a potential range of OCP ± 0.3-0.4 V at a scan rate of 1 mV s^{-1}. The corrosion potential (E_{corr}) and corrosion current density (i_{corr}) were determined by Tafel extrapolation, and the polarization resistance (R_p) was further calculated to quantitatively characterize the anti-corrosion performance of the coatings. The polarization parameters of the different coatings in 3.5 wt.% NaCl solution are summarized in Table S5.

Electrochemical impedance spectroscopy (EIS) measurements were performed in the same electrolyte and three-electrode configuration. An AC perturbation of 10 mV was applied over a frequency range from 10^5 to 10^{-2} Hz, and the Nyquist and Bode plots were recorded near the open-circuit potential. The impedance data were fitted using an equivalent circuit model to obtain the solution resistance (R_s), interfacial charge-transfer resistance (R_2), and the constant phase element (CPE) parameters, thereby enabling a comparative evaluation of the anti-corrosion performance of the different coating interfaces. The EIS fitting parameters of the different coatings in 3.5 wt.% NaCl solution are summarized in Table S6.

2.5 Interfacial stability and self-healing tests

The stability of the PW@LST@E-LIG samples was evaluated using a spin coater (KW-4T, Chinese Academy of Sciences Electronics Co., Ltd., China) operated at 2000 rpm. The mass loss of the surface lubricant was recorded every 10 s, and the corresponding sliding angle (SA) was measured simultaneously. In addition, the anti-scouring performance of the PW@LST@E-LIG samples was assessed by impinging deionized water from a height of 15 cm. The mass loss of the surface lubricant was measured after every cumulative 10 mL of water, and the corresponding variation in SA was recorded. Subsequently, the samples were fixed face-up on a wear tester (Elcometer 1720), where reciprocating sliding was conducted over a stroke length of 5 cm under a brush head load of 100 g. The test was counted in reciprocating cycles of 20 s, and the SA was measured after each cycle. All experiments were repeated five times, and the results are presented as the mean values with standard deviations. To

evaluate the self-healing behavior of the material, the sample surfaces were intentionally damaged with a blade, followed by heating on a hot plate to induce the solid-liquid phase transition of the paraffin wax. The changes in surface morphology were then observed and comparatively analyzed.

2.6 Characterization of physicochemical properties

The surface morphology and elemental composition of the samples were analyzed using a scanning electron microscope (SEM) equipped with energy-dispersive X-ray spectroscopy (EDS) (Quanta 250 FEG, Thermo Fisher Scientific, Waltham, MA, USA). The crystalline structures of the samples were characterized by X-ray diffraction (XRD, Rigaku D/ MAX-2600, Japan) in the 2θ range of 10°-80° with a scanning rate of 10° min^{-1}. In addition, the chemical composition and molecular structure of the samples were investigated by Raman spectroscopy (HR Evolution, Horiba, WJGS-034) and X-ray photoelectron spectroscopy (XPS, Thermo Scientific K-Alpha, USA). Raman spectra were collected over the range of 500-3300 cm^{-1} using a 532 nm laser and a 50× objective lens. The XPS survey spectra were collected over the range of 0-1200 eV. The graphene structure in the prepared LIG was observed by transmission electron microscopy (TEM, Tecnai G2 F20, USA) to verify the successful fabrication of laser-induced graphene. Additionally, the surface morphology of the laser-textured samples was observed using an optical microscope (BX53M, Olympus, Japan).Furthermore, the surface wettability of the coatings was evaluated by measuring the water contact angle and sliding angle using a contact angle meter (JC2000D1, Shanghai Zhongchen Digital Technology Equipment Co., Ltd.).

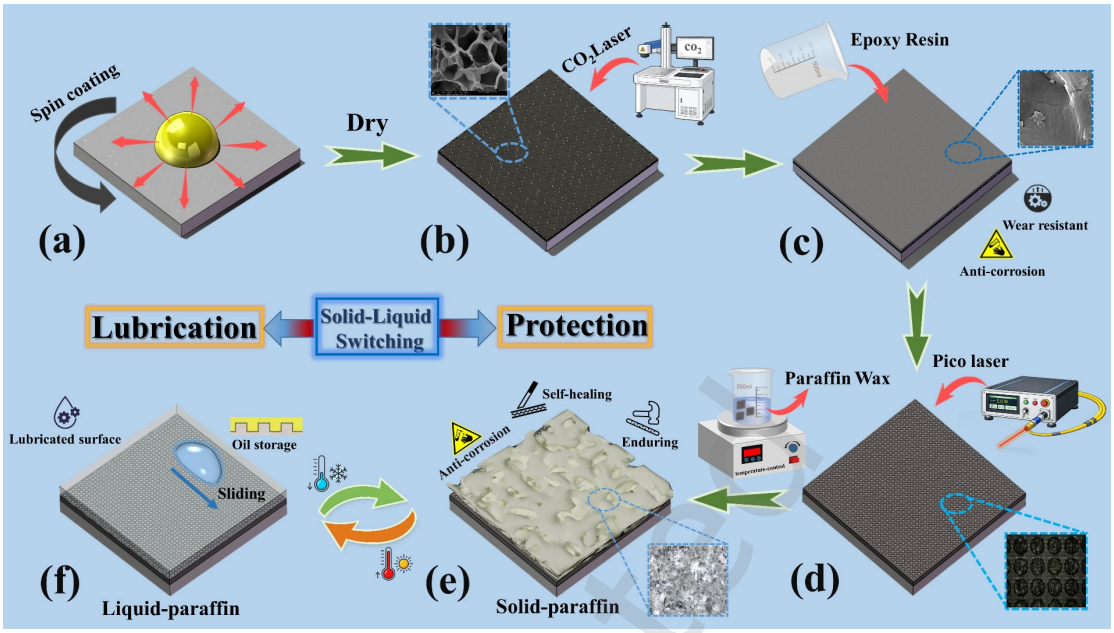

Fig. 1 (a) Preparation of the PI layer. (b) Preparation of LIG. (c) Preparation of E-LIG. (d) Preparation of LST@E-LIG. (e) Preparation of PW@LST@E-LIG and schematic illustration of its solid state. (f) Schematic illustration of the liquid state of PW@LST@E-LIG.

3 Results and Discussion

3.1 Effect of laser parameters on the morphology and properties of LIG

3.1.1 Characterization of LIG

Figs. 2(a)-2(f) present the surface morphologies of LIG prepared at different laser powers (8–18 W). With increasing laser power, the surface gradually evolved from a sparse and relatively dense structure into a typical three-dimensional porous network. At low powers of 8 and 10 W, only a few irregular pores were observed, indicating insufficient carbonization and graphitization of the PI precursor. When the power was increased to 12–14 W, a continuous porous structure was formed, accompanied by the appearance of wrinkled graphitic carbon sheets, suggesting a pronounced enhancement in the graphitization degree. At 16 W, the sample exhibited a well-developed porous

network with relatively uniform pore size and thin pore walls, providing a larger specific surface area. However, when the power was further increased to 18 W, local collapse and ablation became evident, indicating a deterioration in structural integrity.

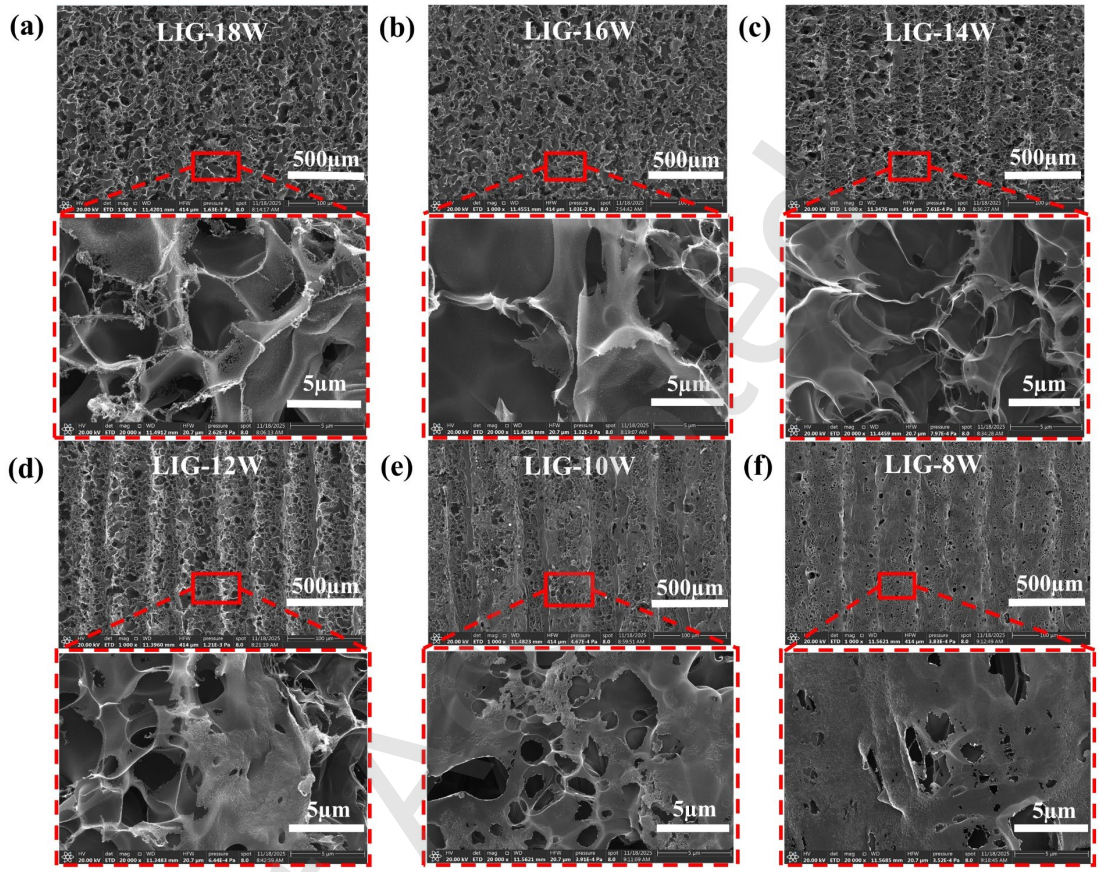

Fig. 2 SEM images of LIG prepared under different laser powers: (a) 18 W, (b) 16 W, (c) 14 W, (d) 12 W, (e) 10 W, and (f) 8 W.

Fig. 3 further reveals the structural evolution of LIG with varying laser power. Fig. 3(a) shows the Raman spectra of the LIG samples at different laser powers. All spectra exhibit distinct D, G, and 2D bands, indicating that the cured polyimide was converted into a graphene-like graphitic carbon structure under laser scanning[40]. Owing to the intrinsic heterogeneous porous structure of LIG, additional Raman measurements were performed on the key LIG samples at 14 W, 16 W, and 18 W, and the average (I_D/I_G) ratios were calculated to compare the differences in graphitization degree. The

additional Raman spectra are shown in Fig. S1. As shown in Fig. 3(b), with increasing laser power, the (I_D/I_G) ratio first increased and then decreased, reaching approximately 1.665 at 10 W, followed by a decrease to the minimum value of approximately 0.250 at 16 W, and then slightly increased to approximately 0.390 at 18 W. This indicates that carbonization is insufficient at relatively low laser powers, resulting in a higher content of disordered carbon and a higher defect density. In contrast, the excessive laser energy input at 18 W causes over-ablation of the LIG structure and introduces more structural defects. Therefore, the LIG16 sample exhibits a higher degree of graphitization than the other samples. As shown in Fig. 3(c), both the atomic and weight percentages of carbon generally increased with laser power and reached their maximum values at 16 W, suggesting that an appropriate energy input promoted the deoxygenation and carbonization of PI, while excessive power could deteriorate the integrity of the carbon framework due to over-ablation.

The graphitic nature of the 16 W sample was further confirmed by the XRD and TEM results shown in Figs. 3(d) and 3(e). Two characteristic diffraction peaks located at approximately 26° and 43° can be assigned to the (002) and (100) planes, respectively, indicating the formation of a typical graphitic carbon structure. In addition, clear lattice fringes were observed in the TEM image, with an interlayer spacing of about 0.34 nm, further evidencing the generation of graphitic microcrystallites. Combined with the XPS results in Figs. 3(f)-3(h), it can be seen that the LIG surface was dominated by C–C bonds, while the oxygen-containing functional groups were significantly reduced, indicating that the laser induction process effectively promoted the conversion of PI

into an sp^2-hybridized carbon structure. Figs. S2-S7 show the EDS spectra of the samples prepared at different laser powers. For all samples, the carbon content increased, whereas the contents of nitrogen and oxygen decreased. These Raman, XRD, and XPS results are consistent with the typical formation mechanism of a three-dimensional porous graphitic carbon network through the rapid deoxygenation and denitrogenation of PI under CO_2 laser irradiation[41, 42]. Overall, the 16 W sample exhibited a higher degree of graphitization and carbonization efficiency, which provided a favorable structural basis for the subsequent improvement in tribological and anti-corrosion performance.

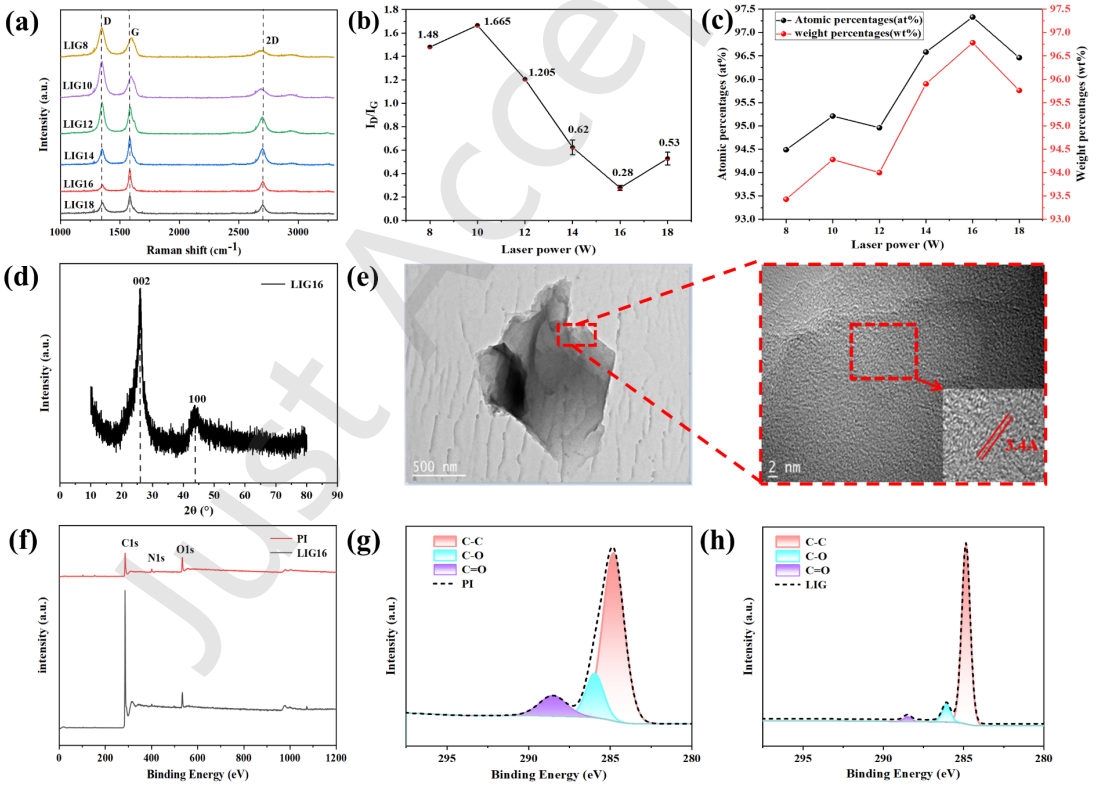

Fig. 3 (a) Raman spectra of the LIG samples. (b) I_D/I_G ratios of the LIG samples prepared at different laser powers. (c) Atomic and weight percentages of carbon. (d) XRD pattern of LIG16. (e) TEM image of LIG16. (f) XPS survey spectra of PI and LIG. (g) High-resolution C1s spectrum of PI. (h) High-resolution C1s spectrum of LIG.

3.1.2 Tribological and anti-corrosion performance of LIG

Figs. 4(a) and 4(b) show the COF of the LIG samples prepared at different laser powers under loads of 1 and 3 N, respectively. The experimental frequency was 2 Hz and the test environmental temperature was 25 °C. All samples underwent an evident running-in stage at the initial period of sliding, followed by a relatively stable friction regime, with the steady-state COF mainly distributed in the range of 0.23–0.27. Under a load of 1 N, the steady-state COF of LIG16 was approximately 0.23. The COF is lower and the fluctuation range is smaller at the initial stage, indicating the tribological performance of LIG16 is superior before the structure is damaged. When the load was increased to 3 N, the COF of all samples increased slightly, while the differences among them became less pronounced; nevertheless, LIG16 and LIG18 COF still maintained relatively slow growth (approximately 20–30% reduction compared to other samples). This result was mainly associated with the effect of laser power on the graphene structure. An appropriate laser power promoted sufficient carbonization of PI and the formation of a continuous three-dimensional porous graphene network, which facilitated the generation of a stable graphene transfer film during sliding, thereby reducing the interfacial shear stress and enabling self-lubrication. In contrast, insufficient graphitization at low power and local over-ablation at excessively high power could both lead to increased friction fluctuations. Fig. 4(c) shows the wear profiles of LIG16 under loads of 1 N and 3 N. The wear depth is close to 100 μm under both 1 and 3 N, which is nearly equivalent to the thickness of the LIG layer. This indicates that the LIG layer was gradually worn during dry sliding and was even close

to being penetrated, suggesting that the wear resistance and long-term structural stability of the single LIG layer were still limited and that further structural optimization was required to improve its service durability.

Fig. 4(d) presents the variation in the water contact angle of the LIG surfaces prepared at different laser powers. With increasing laser power, the contact angle increased from approximately 46° for LIG8 to about 73° for LIG16, corresponding to an increase of about 59%, and then decreased slightly for LIG18. A larger contact angle indicates increased surface hydrophobicity, which is beneficial for suppressing electrolyte retention on the surface and thus can, to some extent, hinder the diffusion of corrosive species toward the substrate.

The samples with a relatively high degree of graphitization were further selected for electrochemical corrosion tests, as shown in Figs. 4(e)-4(i). Compared with the 42CrMo substrate, all LIG samples exhibited improved anti-corrosion performance. The corrosion current densities in the polarization curves decrease (LIG16 decreased by 60.3%), indicating that the LIG layer exerted a certain inhibiting effect on both the anodic dissolution and cathodic reaction. Meanwhile, the corrosion potentials shift positively by approximately 600 mV, suggesting a pronounced reduction in the thermodynamic tendency toward corrosion. The interfacial charge-transfer resistance increase significantly with increasing laser power, reaching approximately 4.809×10^3 Ω cm^2 for LIG16, which is about one order of magnitude higher than that of the substrate (10^2 $\Omega\cdot cm^2$). In the low-frequency region, the Bode modulus increase from about 10^3 $\Omega\cdot cm^2$ for the substrate to nearly 10^4 $\Omega\cdot cm^2$ for LIG16, indicating a markedly

enhanced long-term anti-corrosion performance. In addition, the phase-angle peak increase from approximately 40-50° for the substrate to 75-80° for the LIG-coated samples, and the corresponding frequency range become noticeably broader, suggesting a more ideal capacitive response and improved structural integrity of the coating. Considering both tribological and anti-corrosion performance, 16 W was selected as the optimized laser power for LIG fabrication in this study and was therefore used for the subsequent investigation of the epoxy-infiltrated structure.

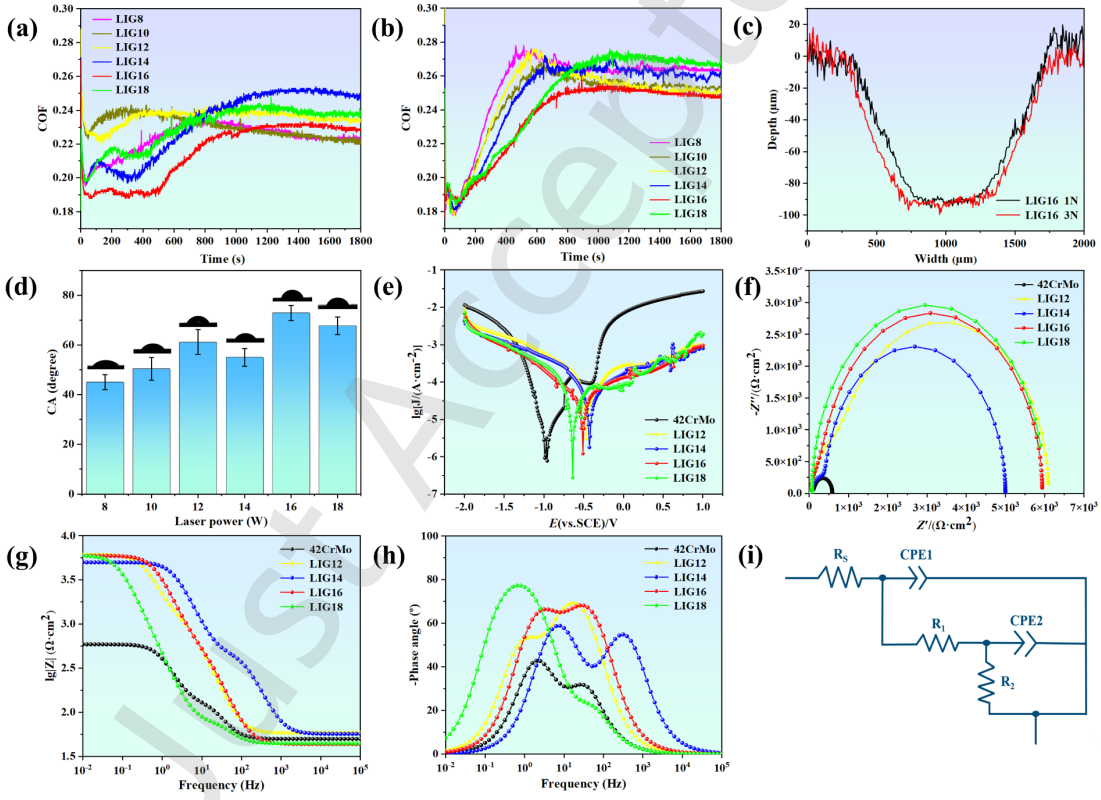

Fig. 4 (a) The COF of the LIG samples under a condition of 1 N, 2 Hz. (b) The COF of the LIG samples under a condition of 3 N, 2 Hz. (c) Wear profiles of LIG16 under loads of 1 and 3 N. (d) Water contact angles of the LIG samples. (e) Polarization curves of the LIG samples. (f) Nyquist plots of the LIG samples. (g) Bode plots of the LIG samples. (h) Phase-angle plots of the LIG samples. (i) Equivalent circuit used for EIS fitting.

3.2 Tribological and anti-corrosion performance of E-LIG

The surface was gradually polished with abrasive paper to expose the complete LIG layer after epoxy infiltration, thereby facilitating the subsequent tribological and anti-corrosion performance tests. Fig. S8 shows the surface morphology of epoxy infiltration laser-induced graphene (E-LIG). As can be seen, the epoxy had fully infiltrated the LIG framework. The corresponding EDS spectra after coating are shown in Fig. S9. A slight decrease in the C content, together with increased N and O contents and a uniform elemental distribution, confirmed the integrity of the epoxy coating. Figs. 5(a) and 5(b) show the COF of the E-LIG samples prepared at different laser powers under loads of 1 and 3 N, respectively. The experimental frequency was 2 Hz and the test environmental temperature was 25 °C. Under a load of 1 N, the steady-state COF of E-LIG16 was approximately 0.36 , representing a reduction of about 35% compared with pure epoxy, whereas E-LIG8 showed a relatively higher value of about 0.50. Compared with the unencapsulated LIG samples (approximately 0.19-0.25), the COF of E-LIG increased slightly, mainly because the epoxy layer bore most of the applied load and reduced the direct sliding contribution of graphene; however, the friction fluctuations were markedly suppressed. When the load was increased to 3 N, the COF of all samples increased by 5-12%. Among them, E-LIG12, E-LIG14, and E-LIG16 remained relatively stable within the range of 0.40-0.50, indicating that the samples prepared at medium laser powers maintained more stable tribological behavior under different loading conditions. This result may be related to the degree of graphene sheet formation. As shown in Fig. 5(c), the maximum wear depth of E-LIG16 under 1 and 3

N is only about 8-12 μm, which is significantly lower than the value of approximately 100 μm observed for the LIG, indicating that the epoxy layer effectively protected the LIG framework and improved the wear stability. This behavior is consistent with the general understanding of polymer composite coatings, in which the resin matrix bears the major load, while the filler framework disperses local stress and enhances interfacial integrity [43].

Fig. 5(d) shows the water contact angles of the E-LIG samples prepared at different laser powers. With increasing laser power, all E-LIG samples exhibited contact angles above 90°(E-LIG16 approximately 100°), indicating good hydrophobicity. Compared with the LIG samples (approximately 46-73°), the water contact angles increased by about 30-70%, which is beneficial for reducing electrolyte retention and suppressing corrosion.

As shown in the polarization curves in Fig. 5(e), the corrosion potentials of the E-LIG samples shift positively by approximately 100-200 mV. The corrosion current densities were 10^{-6} A·cm^{-2} (E-LIG16 was 1.507×10^{-6} A·cm^{-2}), which was about one order of magnitude lower than those of the unencapsulated LIG samples. The Nyquist plots in Fig. 5(f) further indicate a pronounced increase in the interfacial charge-transfer resistance of E-LIG, and the maximum impedance arc radius reached approximately 3.2×10^{4} Ω·cm^2, which was about 3-5 times higher than that of the LIG samples. As shown in Figs. 5(g) and 5(h), the low-frequency impedance modulus reached approximately 10^{5} Ω·cm^2, which was about one order of magnitude higher than that of the LIG samples. Meanwhile, the phase angles were mainly distributed in the range of

60-80°, indicating the formation of a stable and compact protective layer.

Although epoxy infiltration significantly improved the structural stability and anti-corrosion performance, the COF of E-LIG remained slightly higher than that of the LIG (0.25 increased to 0.4), mainly because the epoxy layer bore the applied load and thereby weakened the intrinsic self-lubricating effect of graphene. In addition, prolonged sliding could still induce local wear. To further improve the tribological performance and service stability, it is therefore necessary to introduce a micropore structure while maintaining the integrity of the epoxy layer, so as to provide lubricant storage and sustained release at the interface, thereby reducing the COF and enhancing interfacial stability. Considering the friction, wear, and electrochemical corrosion tests results comprehensively, E-LIG16 was selected as the representative sample for subsequent structural optimization.

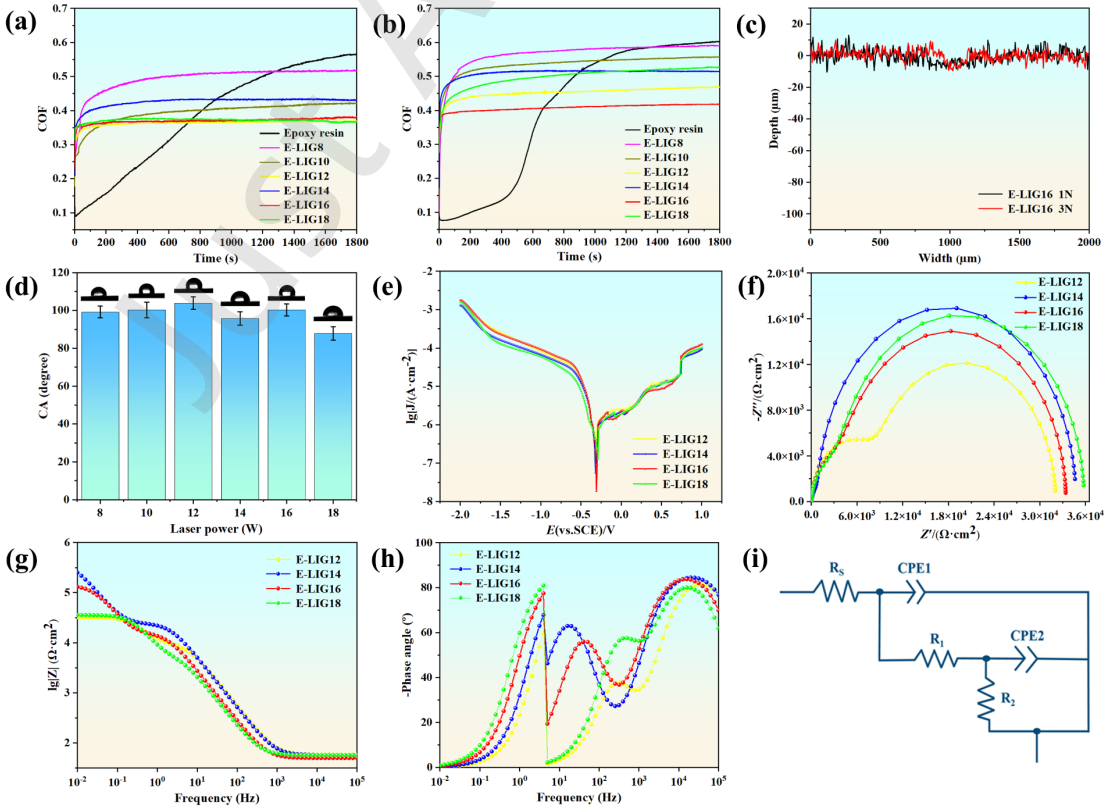

Fig. 5 (a) The COF of the E-LIG samples under a load of 1 N, 2 Hz. (b) The COF of the E-LIG samples under a load of 3 N, 2 Hz. (c) Wear profiles of E-LIG16 under loads of 1 and 3 N. (d) Water contact angles of the E-LIG samples. (e) Polarization curves of the E-LIG samples. (f) Nyquist plots of the E-LIG samples. (g) Bode plots of the E-LIG samples. (h) Phase-angle plots of the E-LIG samples. (i) Equivalent circuit used for EIS fitting.

3.3 Tribological performance of LST@E-LIG

Laser micro-texturing generally provides lubricant storage, debris trapping, and stress redistribution under boundary or mixed lubrication conditions, and its friction-reducing effect is closely related to the texture area density, pore depth, and arrangement pattern[44]. Figs. 6(a)-6(c) show the surface morphologies of micropore arrays with pore-area densities of 20%, 40%, and 50%, respectively. The size of each individual pore remained nearly unchanged (diameter is 400μm), indicating that the laser process enabled stable and controllable fabrication of the microstructures. The corresponding three-dimensional surface morphologies are shown in Figs. 6(d)-6(f), where regularly distributed dimple-like structures can be clearly observed. The pore depths were essentially the same for all samples (approximately 100μm), suggesting that only the number of micropores changed under different area densities, whereas the pore geometry remained stable. This provided a reliable structural basis for the subsequent analysis of the effect of area density on tribological behavior.

Fig. 6(g) shows the SEM morphology of the sample with a 40% area density. The micropores exhibited clear boundaries, and layered textures generated by laser scanning were retained inside the pores, which is beneficial for enhancing the adhesion and

retention of lubricants within the pores. Combined with the cross-sectional morphology shown in Fig. 6(h), it can be further confirmed that the depth of laser-fabricated micropores extended exactly to the bottom of the epoxy layer (approximately 100 μm, total thickness is approximately 200 μm), resulting in the local exposure of the LIG structure at the pore bottom, while the surrounding regions remained fully covered by the epoxy layer. Fig. S10 presents the EDS elemental content and distribution across the micropore cross-section. Such a structure can maintain the overall integrity of the coating while locally providing a lubricating-active LIG phase, thereby enabling solid lubrication during sliding.

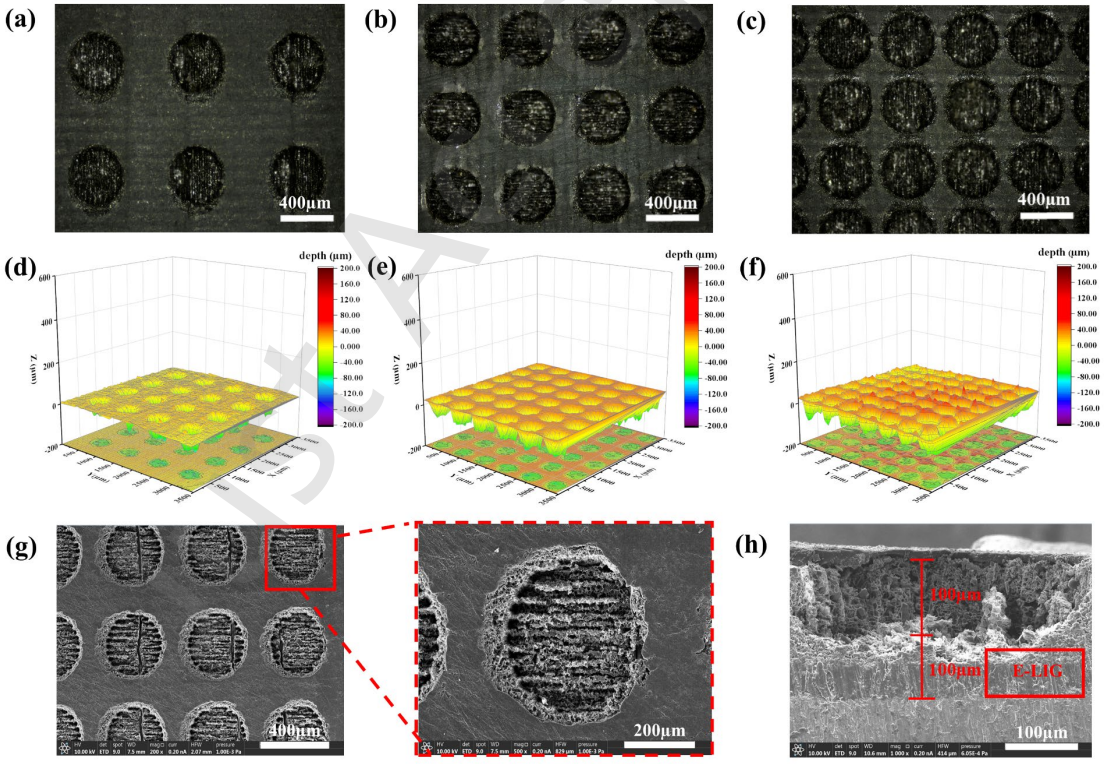

Fig. 6 Optical micrographs of samples with different pore-area densities: (a) 20%, (b) 40%, and (c) 50%. Three-dimensional surface profiles of samples with different pore-area densities: (d) 20%, (e) 40%, and (f) 50%. (g) SEM image of the sample with a 40% pore-area density and its enlarged view. (h) Cross-sectional profile of the micropore.

Figs. 7(a)-7(c) indicate that the pore-area density played a significant role in regulating the tribological response of the E-LIG surface. Tribological performance tests were conducted on samples of different densities at loads of 3 N, 5 N, and 10 N respectively. The experimental frequency was 2 Hz and the test environmental temperature was 25 °C. Under loads of 3 and 5 N, all three textured samples exhibited lower COF than the untextured surface, among which the samples with 40% and 50% pore-area densities showed relatively lower steady-state COF. In the 40% pore-area density, the COF is 50% lower than E-LIG and 66% lower than epoxy (Reduced to around 0.2). This suggests that, with increasing pore coverage, more lubricant-storage units were introduced, making it easier for the interface to establish a relatively continuous lubricating state. By contrast, although the sample with a 20% area density also exhibited a reduced COF (approximately 0.24), its lubricant-storage and release capacities were still limited due to the smaller number of micropores.

When the load was further increased to 10 N, the differences among the samples with different pore-area densities became more pronounced. The samples with 20% and 40% pore-area densities both reached a relatively stable state after a short running-in period, with the COF remaining at approximately 0.25-0.26, whereas that of the 50% pore-area density sample continuously increased to about 0.44. This indicates that, under high-load conditions, although a higher pore coverage is beneficial for lubricant storage, it also markedly reduces the continuous load-bearing area, resulting in increased local contact stress and a consequent weakening of the stability of the surface framework, thereby making the friction process more prone to instability. Therefore, the lubricant-

storage advantage introduced by increasing the pore-area density does not always translate into more stable friction-reducing performance, as the final effect is also jointly governed by the load-bearing area and the structural integrity of the surface.

Fig. 7(d) further compares the original cross-sectional profile of the dimples with that measured after sliding under a load of 5 N for the sample with a 40% area density. Periodic dimple-like undulations could still be clearly distinguished after wear, indicating that the micropore structure was not completely destroyed during the friction process and that a certain number of lubricant-storage units were still retained. This suggests that the micropore structure was capable of effectively storing lubricants while maintaining a certain degree of structural stability, thereby facilitating the formation of a stable lubricating state and mitigating surface wear.

To further quantitatively evaluate the lubrication property of the micropore structure, its lubricant-storage capacity can be assessed by calculating the volume available for lubricant retention. For a regularly arranged array of cylindrical micropores, the storage volume of a single micropore can be expressed as:

$$\boldsymbol{V_P = \pi r^2 h} \tag{1}$$

where r is the radius of the micropore and h is the depth of the micropore. When the number of micropores per unit area is n, the total lubricant storage volume per unit area can be expressed as:

$$\boldsymbol{V_{total} = n\pi r^2 h} \tag{2}$$

The calculated total lubricant-storage volumes are summarized in Table S4. As the area density increased, the volume of lubricant that could be stored per unit area

increased markedly. However, when the pore-area density became excessively high, although the lubricant-storage capacity was further enhanced, the effective load-bearing area of the surface was significantly reduced. Therefore, a balance must be achieved between lubricant-storage capability and interfacial load-bearing capacity in the design of the micropore structure. The nominal Hertzian contact pressure was further estimated to evaluate the contact degree during sliding, and the detailed calculation is provided in Table S7. Although the laser-textured surface exhibits a higher corrected nominal contact pressure due to the reduced effective load-bearing area, its COF is lower than that of the untextured E-LIG surface. This indicates that the tribological behavior is not governed solely by Hertzian contact pressure. The reduced COF of LST@E-LIG is mainly attributed to the structural effects of the micropores, including debris trapping, contact-state regulation, reduced effective contact area, and partial exposure of the underlying LIG phase. The locally exposed LIG can provide graphitic lubricating species through slight wear and transfer-film formation, thereby lowering the interfacial shear resistance. Meanwhile, the micropores also provide reserved storage sites for the infiltration of paraffin wax.

Overall, the 40% pore-area density achieved a more favorable balance between lubricant-storage and load-bearing capacity, and therefore exhibited relatively low and stable COF under different loading conditions. Accordingly, it was selected as the optimal structural parameter for the subsequent paraffin wax infiltration experiments.

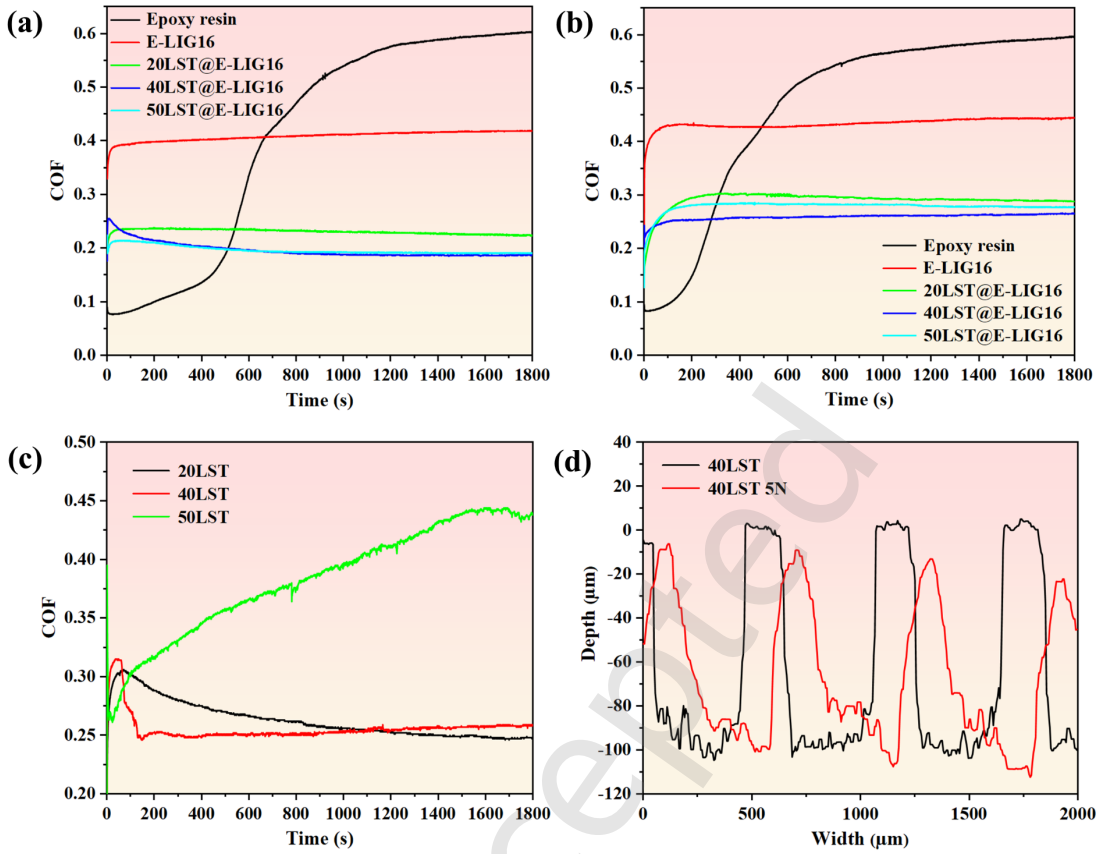

Fig. 7 The COF of samples with different pore-area densities under conditions of (a) 3 N, 2 Hz, (b) 5 N, 2 Hz, and (c) 10 N, 2 Hz. (d) Cross-sectional profile of the dimples with a 40% pore-area density before and after sliding under a load of 5 N.

3.4 Tribological and anti-corrosion performance of PW@LST@E-LIG

3.4.1 Tribological performance of PW@40LST@E-LIG16

Fig. 8(a) shows the SEM morphology of solid paraffin wax, which exhibits a bird's-nest-like network structure internally, resembling an interwoven assembly of soil and branches. This morphology enables strong mechanical interlocking with the interior of the micropores, making it less prone to detachment. Owing to its unique three-dimensional interconnected architecture, the applied load can be effectively dispersed and local stress concentration can be reduced, thereby significantly improving the mechanical stability and durability of the surface coating. Fig. S11 shows the cross-

sectional morphology after paraffin wax infiltration, indicating that the paraffin wax fully filled the micropores and was well interlocked with the internal structure. Fig. 8(b) schematically illustrates the friction process after paraffin wax infiltration.

Figs. 8(c) and 8(d) compare the tribological responses of the 40PW@40LST@E-LIG16 system under solid-state and liquid-state conditions under a load of 3 N. The experimental frequency was 2 Hz. The test temperature under solid condition was 25 °C, and the test temperature under liquid conditions is 45 °C. After paraffin wax infiltration, the COF decreased further, and the COF of the liquid-state condition (approximately 0.11) was 20% lower than that under the solid-state condition (approximately 0.13). This suggests that the friction-reducing effect of paraffin wax originated not only from pore filling, but was also closely associated with the formation of a continuous low-shear lubricating film at the sliding interface after melting. To further support the thermally responsive lubrication mechanism, we conducted a solid-liquid phase-transition tribological test and added infrared thermal imaging measurement data, as shown in Fig. 8(e). The process can be divided into three stages: solid state, solid-liquid transition state, and liquid state. In the initial solid-state stage, the near-contact surface temperature remained at approximately 27-28 °C, below the phase-transition temperature of paraffin wax. At this stage, the paraffin wax mainly acted as a filling and protective phase, and the COF gradually decreased and stabilized after running-in. After heating was applied, the temperature increased at an average rate of 5 °C·min^{-1} and reached the phase-transition temperature. When the temperature near the wear track reached approximately 40 °C, the COF decreased markedly, indicating that the softened

paraffin wax formed a low-shear lubricating film. The temporary COF fluctuation during the solid-liquid transition stage may be attributed to the dynamic redistribution of paraffin wax and reconstruction of the lubricating film. In the final liquid-state stage, the temperature remained above the phase-transition temperature, and the COF stabilized at a low level of approximately 0.08, suggesting continuous spreading and replenishment of liquid paraffin wax at the sliding interface. It should be noted that the infrared thermal images reflect the near-contact surface temperature rather than the instantaneous flash temperature at real asperity contacts. Overall, the infrared thermal imaging results, together with the corresponding COF evolution, provide strong evidence for the thermally responsive lubrication mechanism involving paraffin wax melting, release, spreading, and replenishment. In addition, we added comparative macroscopic optical morphology images of 40PW@40LST@E-LIG16 before and after the solid-liquid phase-transition tribological test (Fig. S12). Before the test, the solid paraffin wax covered the textured surface and filled and covered the micropores, indicating that the micropores could act as storage and confinement sites. After the solid-liquid transition and sliding, obvious paraffin wax redistribution and a visible wear track were observed, suggesting that the melted paraffin wax participated in the sliding process and migrated toward the contact region rather than being simply removed from the surface. In addition, the dynamic motion of the surface paraffin during the solid-to-liquid transition and subsequent re-spreading process was recorded by video, as shown in Video S1.

In addition, tribological tests were conducted under higher load and frequency

conditions (10 N and 3 Hz) without ambient-temperature control to determine whether the actual contact temperature during sliding could reach the melting point of the paraffin wax. Real-time infrared thermal images and optical images were recorded, as shown in Fig. S13. As shown in Fig. S13(a), the initial temperature of the sample was controlled at approximately 16 °C, at which the paraffin wax with a phase-transition temperature of 20 °C still remained in the solid state. After a short period of sliding, the surface temperature approached the melting point after approximately 5 min under the combined effects of ambient temperature and frictional heating. After 30 min of sliding, the surface temperature increased to 27.5 °C, and the paraffin wax completely transformed into the liquid state. As shown in Fig. S13(b), for the sample containing paraffin wax with a melting point of 40 °C, the surface temperature reached approximately 30 °C after about 20 min of sliding and increased to 31.2 °C at the end of the 30 min test. The surface temperature increased by approximately 5 °C, but it did not reach the melting point; therefore, the paraffin wax in the wear track remained in the solid state. As shown in Fig. S13(c), for the sample containing paraffin wax with a melting point of 60 °C, the frictional heat generated during sliding was relatively lower, which may be associated with its slightly lower solid-state COF. Accordingly, the temperature-rise rate was also relatively slower. The surface temperature reached 28.1 °C after approximately 25 min and increased to 29.9 °C at the end of the 30 min test. The surface temperature increased by approximately 4 °C, which was still below the melting point of this paraffin wax. These results indicate that, under higher load and frequency sliding conditions, frictional heat was indeed generated during sliding,

leading to a certain increase in surface temperature. However, paraffin wax with a higher melting point requires more severe testing conditions to trigger the solid-liquid phase transition.

Moreover, to simulate the property under harsh working conditions, we tested the tribological performance of PW@40LST@E-LIG16 at varying loads and frequencies (Load: 2 N-10 N, Frequency: 2 Hz-5 Hz). The frequency was kept constant at 2 Hz for the tests under different loads, while the load was kept constant at 2 N for the tests with different frequencies. As shown in Figs. 8(f) and 8(h), the average COF generally increased with increasing frequency (0.12 to 0.17). This indicates that a higher number of cycles per unit time accelerated the disruption of the lubricating film, making it difficult for the paraffin wax replenishment rate to keep pace with film consumption. Nevertheless, the overall friction level remained relatively low and stable. (the COF remains at 0.14). Figs. 8(g) and 8(i) show the COF and the average COF under different loads, all of which exhibited distinct running-in and steady-state stages. With increasing load, the COF gradually decreased and became more stable. In particular, the average COF slightly decreased from about 0.13 to approximately 0.09 as the load increased, suggesting that an appropriate increase in the normal pressure facilitated paraffin wax extrusion, compaction of the transfer film, and the rapid establishment of the interfacial lubricating layer.

Overall, the low-friction behavior of this system did not arise from the texture effect alone, but was governed by a dynamic and adaptive lubrication process involving micropore storage, paraffin wax release, and interfacial film formation. As a result, the

lubrication performance was significantly improved, and the system was endowed with good environmental adaptability.

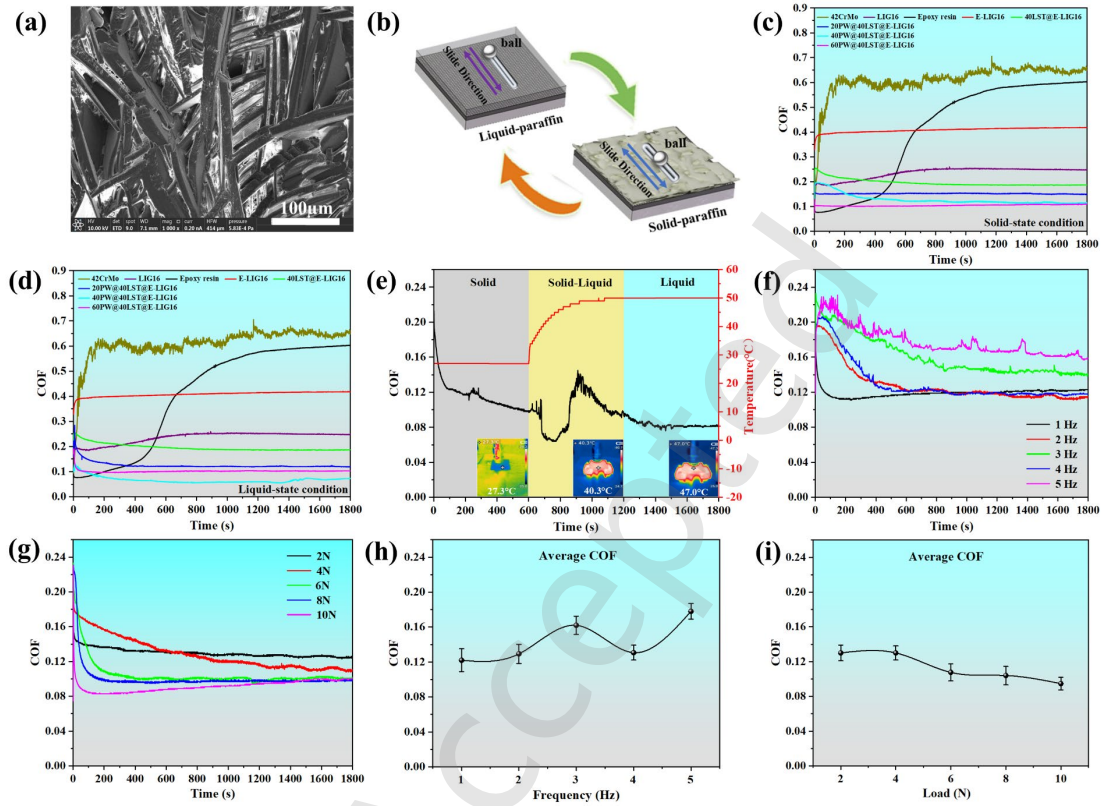

Fig. 8. (a) SEM image of solid paraffin wax. (b) Schematic illustration of the tribological performance tests under solid-state and liquid-state conditions. (c, d) The COF of PW@40LST@E-LIG16 under solid-state (25 °C) and liquid-state (45 °C) conditions (3 N, 2 Hz). (e) The COF of 40PW@40LST@E-LIG16 during the solid-liquid phase-transition process under condition of 3 N, 2 Hz. (f, g) The COF of 40PW@40LST@E-LIG16 under different frequencies (1-5 Hz) and loads (2-10 N). (h, i) Average COF of 40PW@40LST@E-LIG16 under different frequencies and loads.

3.4.2 Surface stability of PW@40LST@E-LIG16

To further evaluate the stability and durability of the paraffin wax lubricating layer under complex environmental conditions, anti-shear, anti-scouring, and anti-wear tests were conducted, and the self-healing ability and cyclic stability were analyzed. As

shown in Fig. 9(a), centrifugal shearing, deionized-water scouring, and reciprocating friction were employed to simulate shear stress, liquid impingement, and frictional wear encountered in practical service environments, respectively, thereby enabling a systematic evaluation of the stability of the paraffin wax reservoir layer.

The stability of the lubricant under different test conditions was quantitatively assessed in terms of the mass retention ratio:

$$\boldsymbol{R = \frac{m_t}{m_0} \text{x} 100\%} \tag{3}$$

where m_o is the initial mass, m_t is the remaining mass after testing, and R represents the mass retention ratio of the lubricant.

As shown in Fig. 9(b), under centrifugal shearing, the mass retention ratio of liquid paraffin wax gradually decreased from 100% to approximately 63% with increasing centrifugation time due to its relatively high fluidity. However, the destruction of the surface oil film exposed the underlying micropore structure, creating anchor points that hinder the sliding of the droplets, whereas solid paraffin wax exhibited almost no mass loss throughout the entire process and remained close to 100%. This difference can be attributed to the mechanical interlocking effect of the micropore structure, which allowed the solid paraffin wax to be stably anchored within the pores and thus effectively resist the applied shear force. Correspondingly, as shown in Fig. 9(c), the sliding angle (SA) of liquid paraffin wax increased from about 5° to approximately 10°, indicating that continuous shearing weakened the continuity of the liquid lubricating layer, whereas the SA of solid paraffin wax remained around 90° throughout the test, suggesting stronger interfacial adhesion stability of the solid-state paraffin wax.

As shown in Figs. 9(d) and 9(e), when the amount of deionized water used for scouring increased to 100 mL, the mass retention ratio of liquid paraffin wax further decreased to about 54%, while the sliding angle increased from approximately 5° to around 15°. In contrast, solid paraffin wax still maintained a mass retention ratio close to 100% together with a stable wetting state. This indicates that, unlike liquid paraffin wax, which mainly relies on the adhesion of the interfacial lubricating film, solid paraffin wax was much less likely to be lost under external forces and liquid impingement, and therefore exhibited better environmental stability. To evaluate the wear resistance, reciprocating anti-wear tests were further performed, as shown in Fig. 9(f). As the time increased from 0 s to 100 s, the mass retention ratio of solid paraffin wax decreased from 100% to approximately 74%, indicating that mechanical wear continuously consumed the paraffin wax on the outermost surface. However, the decrease remained relatively gradual, suggesting that the solid paraffin wax still possessed a certain resistance to wear.

In addition, as shown in Fig. 9(g), the wear scratches generated during friction could be completely recovered after heating. This phenomenon indicates that the system exhibited a typical phase-transition-driven self-repair characteristic, in which the molten paraffin wax re-spread and repaired the damaged areas under the combined action of capillary force and surface tension. As shown in Fig. 9(h), the contact angle and sliding angle of the 20 °C paraffin wax exhibited stable periodic variations during repeated solid-liquid transitions. The peak and valley values remained essentially unchanged over multiple cycles, with no obvious attenuation observed, indicating that

the system was able to repeatedly reconstruct its surface wetting state under phase-transition driving. The cyclic stability of paraffin waxes with different phase-transition temperatures is shown in Figs. S14 and S15, all of which exhibited good stability, thereby providing an effective strategy for constructing long-term stable self-lubricating surfaces. Overall, the paraffin wax in this system not only provided lubrication, but also endowed the surface with good resistance to external disturbances and reversible self-healing capability.

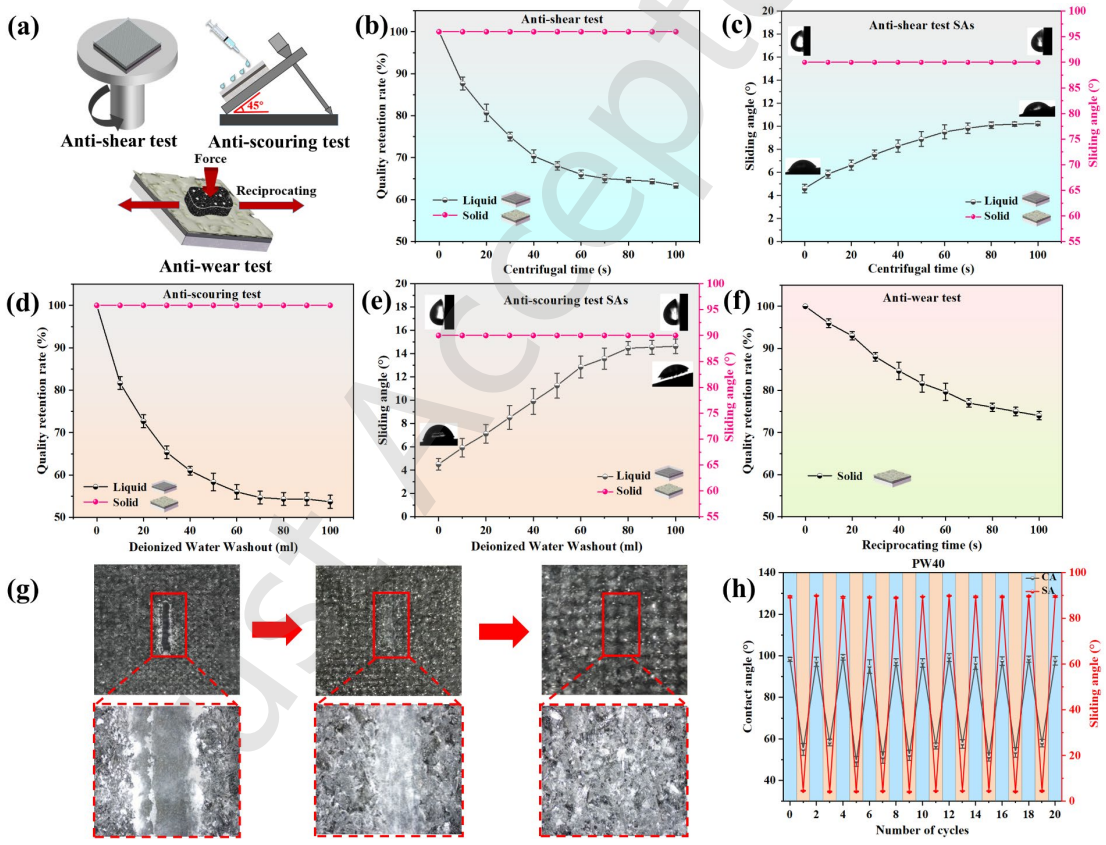

Fig. 9. (a) Schematic illustrations of the anti-shear, anti-scouring, and anti-wear tests. (b) Mass retention ratio during the anti-shear test. (c) Variation in the sliding angle (SA) during the anti-shear test. (d) Mass retention ratio during the anti-scouring test. (e) Variation in the sliding angle (SA) during the anti-scouring test. (f) Mass retention ratio during the anti-wear test. (g) Surface morphologies before and after the self-healing test. (h) Variations in the contact angle (CA) and

sliding angle (SA) of the 40 °C paraffin wax during repeated solid-liquid transitions.

3.4.3 Tribological and anti-corrosion synergistic effect

To further clarify the effects of different surface structures on the friction, wear, and corrosion behaviors, the wear-track morphologies and electrochemical corrosion were systematically characterized. Figs. 10(a) and 10(b) present the three-dimensional profiles and SEM images of the wear tracks on different surfaces under condition of 3 N, 2 Hz. LIG16 exhibited a relatively wide and continuous wear track with clearly defined groove boundaries, indicating that bare LIG was more susceptible to direct shear and material removal during sliding. After epoxy infiltration, the wear track of E-LIG16 became noticeably narrower, and the surface continuity was improved, suggesting that the infiltration layer could alleviate local stress concentration and enhance interfacial stability. Upon the further introduction of micropores with a 40% pore-area density, regular dimple contours could still be distinguished within the wear track of 40LST@E-LIG16, indicating that the textured units were not completely worn away during sliding. Its friction-reducing effect was mainly attributed to debris entrapment, reduction of the real contact area, and redistribution of contact stress. In contrast, the wear track of PW@40LST@E-LIG16 under a load of 3 N was much smoother, with significantly weakened groove features. A relatively continuous covering layer could be observed in the SEM image, indicating that paraffin wax formed a lubricating transfer film at the interface, thereby further suppressing adhesive wear and ploughing. Fig. S16 shows the three-dimensional wear-track profile under condition of 10 N,2 Hz. Even under relatively high loads, the textured surface still

maintained a certain degree of structural integrity. This indicates that a synergistic effect was established between the load-bearing micropore structure and the dynamic replenishment of paraffin wax. This suggests that a synergistic effect was established between the load-bearing micropore structure and the dynamic replenishment of paraffin wax.

To evaluate the influence of paraffin wax infiltration on the anti-corrosion performance of the composite coating, electrochemical measurements were performed on the solid-state paraffin wax samples, as shown in Fig. 10(c). The polarization curves indicate that the corrosion current density decreased by about one order of magnitude relative to that of E-LIG (decreased to 10^{-7} A·cm^{-2}), while corrosion potential shifted positively by approximately 300 mV, indicating that the corrosion reaction was effectively suppressed and the corrosion tendency was reduced. The Nyquist plots further demonstrate that the paraffin wax samples exhibited a significantly enlarged impedance arc radius, corresponding to a pronounced increase in the interfacial charge-transfer resistance, which was approximately four times that of E-LIG (reached 10^5 Ω·cm^2). In the Bode plots, the paraffin wax samples exhibited a higher impedance modulus in the low-frequency region (10^7 Ω·cm^2), indicating a stronger resistance to the diffusion of corrosive ions. Meanwhile, the phase angle remained at a relatively high level over a broader frequency range, suggesting a more stable capacitive response and a protective layer with higher integrity and compactness.

To clarify the synergistic mechanism, the individual contribution of each structural component was further distinguished through a control matrix (Table S8). First, LIG

provides a graphitic solid-lubricating phase and a carbon-based barrier, which reduce interfacial shear and partially improve corrosion resistance. However, the bare LIG framework is mechanically fragile and can be worn through during sliding. Second, epoxy infiltration reinforces and seals the porous LIG framework, significantly improving wear resistance and corrosion protection, although the COF slightly increases because the epoxy layer bears most of the applied load and weakens the direct lubricating contribution of graphene. Third, laser surface texturing introduces ordered micropore arrays. By tuning the laser processing parameters, the ablation depth is optimized, enabling partial exposure of the underlying LIG layer, which facilitates the release of graphitic species during sliding, redistributes local contact stress, and provides additional lubricant storage sites. Fourth, paraffin wax serves as a low-shear lubricating phase and enables thermally responsive lubricant release, diffusion, and replenishment at the sliding interface. Therefore, the optimized PW@LST@E-LIG surface should not be regarded as a simple hydrophobic barrier; rather, its enhanced tribological and anti-corrosion performance arises from the synergistic coupling of LIG solid lubrication, epoxy infiltration, micropore-based lubricant-storage structure, paraffin wax lubrication, and hydrophobic/barrier protection. In Table S9, the PW@LST@E-LIG coating was compared with recently reported solid-lubricating materials, LIG-based coatings, graphene-containing textured surfaces, phase-change lubrication systems, and anti-corrosion/anti-wear composite coatings. This multilevel-structured design overcomes the limitations of single-function coatings by integrating solid lubrication, structural reinforcement, lubricant storage, thermally responsive

replenishment, and corrosion protection into one hierarchical coating, thereby achieving synergistically enhanced tribological and anti-corrosion performance. The corresponding schematic diagram illustrating the tribological and anti-corrosion mechanisms is shown in Fig. 11.

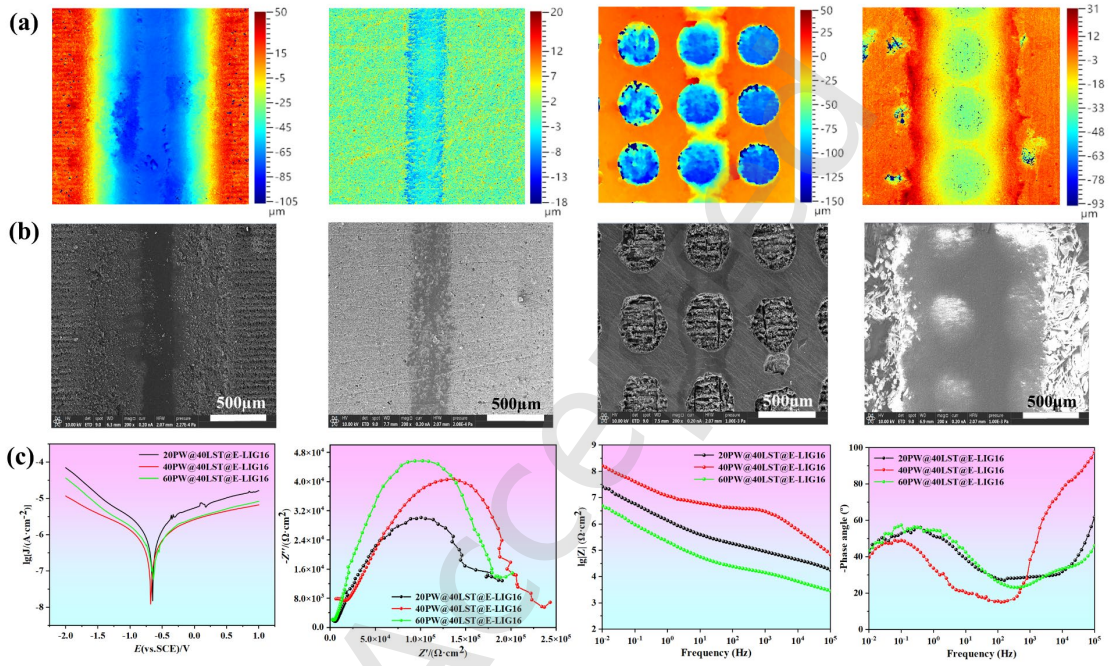

Fig. 10 (a) Three-dimensional wear-track profiles of LIG16, E-LIG16, 40LST@E-LIG16, and 40PW@40LST@E-LIG16 under condition of 3 N, 2 Hz. (b) SEM images of the wear tracks. (c) Polarization curve, Nyquist plot, Bode plot, and phase-angle plot of 20, 40, 60PW@40LST@E-LIG16.

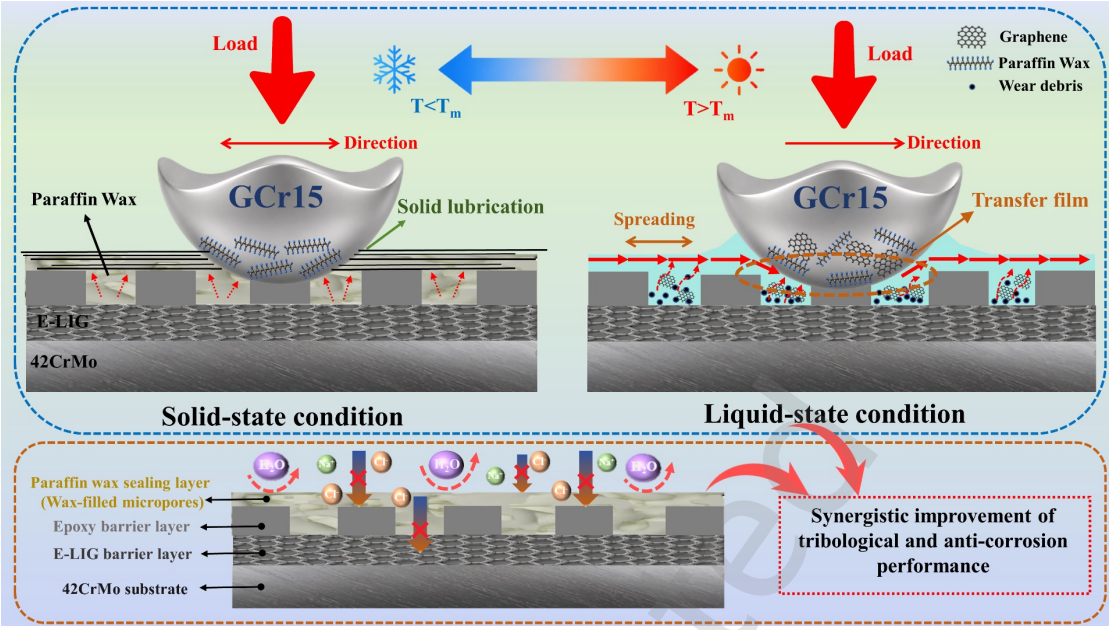

Fig. 11 Schematic diagram of the tribological and anti-corrosion mechanisms.

4. Conclusion

In this work, a multilevel-structured phase-responsive solid-liquid composite lubricating coating was developed to address the synergistic failure caused by friction, wear, and corrosion under complex service conditions. The test results showed that the LIG at a laser power of 16 W (corresponding to a laser energy density of 20.38 J cm^2) possessed a porous network with more uniform pore size and thinner pore walls, as well as a higher degree of graphitization. This structure provided a larger specific surface area and, through combination with epoxy, effectively improved the wear resistance of the coating, reducing the wear depth by approximately 90%, while also enhancing its anti-corrosion performance, with the inhibition efficiency reaching approximately 96%. After laser surface texturing, a favorable balance between lubricant-storage capacity and structural strength was achieved when the pore-area density of the micropore array was 40%. Under this condition, the COF was reduced by 50% compared with E-LIG

and by 66% compared with pure epoxy, reaching approximately 0.2. After the introduction of paraffin wax, a dynamically adaptive lubricating film with solid-liquid transition characteristics was formed on the surface, which effectively reduced the interfacial shear stress, resulting in low COF of 0.09. Meanwhile, the paraffin wax and epoxy layer synergistically formed a dense barrier, thereby significantly enhancing the anti-corrosion performance (the interfacial charge-transfer resistance reached 10^5 $\Omega \cdot cm^2$, the corrosion current density reached 10^{-7} $A \cdot cm^{-2}$, the corrosion current density decreased by more than two orders of magnitude compared with that of the substrate, resulting in an inhibition efficiency of 99.54%). Through this stepwise design strategy of "structural construction-parameter optimization-functional coupling," the synergistic improvement of tribological and anti-corrosion performance was successfully achieved.

ASSOCIATED CONTENT

Acknowledgments

The authors acknowledge the support by the National Key R&D Project of China (Grant No. 2024YFB4608400), the National Natural Science Foundation of China (52575342, 52205313), the Tribology Science Fund of State Key Laboratory of Solid Lubrication (LSL-2312), Scientific Innovation Project for Young Scientists in Shandong Provincial Universities (2023KJ145).

Declaration of Competing Interest

The authors declare that they have no known competing financial interests or personal relationships that could have appeared to influence the work reported in this paper.

References

[1] Cao S F, Mischler S. Modeling tribocorrosion of passive metals - A review. *Curr Opin Solid State Mat Sci* **22**(4): 127–141 (2018)

[2] Holmberg K, Erdemir A. Influence of tribology on global energy consumption, costs and emissions. *Friction* **5**(3): 263–284 (2017)

[3] Meng Y G, Xu J, Jin Z M, Prakash B, Hu Y Z. A review of recent advances in tribology. *Friction* **8**(2): 221–300 (2020)

[4] Ou B L, Wang Y W, Lu Y. A review on fundamentals and strategy of epoxy-resin-based anticorrosive coating materials. *Polym-Plast Tech Mater* **60**(6): 601–625 (2021)

[5] Wang A N, De Silva K, Jones M, Robinson P, Larribe G, Gao W. Anticorrosive coating systems for marine propellers. *Prog Org Coat* **183**: 107768 (2023)

[6] Ge X Y, Chai Z Y, Shi Q Y, Liu Y F, Wang W Z. Graphene superlubricity: A review. *Friction* **11**(11): 1953–1973 (2023)

[7] Sinclair R C, Suter J L, Coveney P V. Graphene-Graphene Interactions: Friction, Superlubricity, and Exfoliation. *Adv Mater* **30**(13): 1705791 (2018)

[8] Sun J L, Du S N. Application of graphene derivatives and their nanocomposites in tribology and lubrication: a review. *RSC Adv* **9**(69): 40642–40661 (2019)

[9] Avinash K, Patolsky F. Laser-induced graphene structures: From synthesis and applications to future prospects. *Mater Today* **70**: 104–136 (2023)

[10] Li J T, Stanford M G, Chen W Y, Presutti S E, Tour J M. Laminated Laser-Induced Graphene Composites. *Acs Nano* **14**(7): 7911–7919 (2020)

[11] Wang Z W, Liu W C, Yuan W, Cong J C, Chander P, Wu L Y, Zheng H Y. The effect of laser in-situ

induced graphene-like micro-texture on the friction and wear properties of ductile cast iron. *J Mater Res Technol-JMRT* **12**: 2407–2413 (2021)

[12] Ye R Q, James D K, Tour J M. Laser-Induced Graphene. *Accounts Chem Res* **51**(7): 1609–1620 (2018)

[13] Xue P D, Huang Z Q, Chen C. Effect of Substrate Roughness on the Friction and Wear Behaviors of Laser-Induced Graphene Film. *Lubricants* **10**(10): 239 (2022)

[14] Wang L Y, Liu M M, Yadav A, Wu Y L, Zheng H Y. A method for preparing and investigating anti-/de-icing surface by integration of laser-induced graphene (LIG) with a silica sol adhesive (SMP@M-SiO2). *Surf Coat Technol* **474**: 130111 (2023)

[15] Teng S, Gao Y, Cao F L, Kong D B, Zheng X Y, Ma X M, Zhi L J. Zinc-reduced graphene oxide for enhanced corrosion protection of zinc-rich epoxy coatings. Prog Org Coat **123**: 185–189 (2018)

[16] Xu H Y, Lu D, Han X. Graphene-induced enhanced anticorrosion performance of waterborne epoxy resin coating. *Front Mater Sci* **14**(2): 211–220 (2020)

[17] Zhang R Y, Yu X, Yang Q W, Cui G, Li Z L. The role of graphene in anti-corrosion coatings: A review. *Constr Build Mater* **294**: 123613 (2021)

[18] Zhao H R, Ding J H, Zhou M, Yu H B. Enhancing the Anticorrosion Performance of Graphene-Epoxy Coatings by Biomimetic Interfacial Designs. *ACS Appl Nano Mater* **4**(7): 6557–6561 (2021)

[19] Zhou Y, Li Q, Atrens A, Wu L. Graphene-based anti-corrosion coatings on magnesium alloys: a review. *Surf Eng* **39**(4): 392–412 (2023)

[20] Batista P F R, Koga H H, Campideli V C, Sicupira D C, Santos L D. Anti-Corrosion and Mechanical Performance of Graphene Oxide and Reduced Graphene Oxide Multi-Layer Coatings Applied to Nickel-Titanium Via Dip-Coating. *Mater Res-Ibero-am J Mater* **28**: e20240483 (2025)

[21] Hashemi M M, Hahseminia F, Sadeghzadeh S. Alkyd coated laser induced graphene patches for corrosion resistance of metal substrates. *Sci Rep* **15**(1): 31453 (2025)

[22] Chen K Y, Tang Y Q. Research Progress on the Design of Surface Texture in Tribological Applications: A Mini-Review. *Symmetry-Basel* **16**(11): 1523 (2024)

[23] Grützmacher P G, Profito F J, Rosenkranz A. Multi-Scale Surface Texturing in Tribology-Current Knowledge and Future Perspectives. *Lubricants* **7**(11): 95 (2019)

[24] Kumar V, Verma R, Kango S, Sharma V S. Recent progresses and applications in laser-based surface texturing systems. *Mater Today Commun* **26**: 101736 (2021)

[25] Rosenkranz A, Costa H L, Baykara M Z, Martini A. Synergetic effects of surface texturing and solid lubricants to tailor friction and wear - A review. *Tribol Int* **155**: 106792 (2021)

[26] Vishnoi M, Kumar P, Murtaza Q. Surface texturing techniques to enhance tribological performance: A review. *Surf Interfaces* **27**: 101463 (2021)

[27] Yue H Z, Schneider J, Deng J X. Laser Surface Texturing for Ground Surface: Frictional Effect of Plateau Roughness and Surface Textures under Oil Lubrication. *Lubricants* **12**(1): 22 (2024)

[28] Zhang J J, Zhang J G, Rosenkranz A, Zhao X L, Song Y L. Surface Textures Fabricated by Laser Surface Texturing and Diamond Cutting - Influence of Texture Depth on Friction and Wear. *Adv Eng Mater* **20**(4): 1700995 (2018)

[29] Cao Z F, Xia Y Q, Chen C, Zheng K, Zhang Y. A synergetic strategy based on laser surface texturing and lubricating grease for improving the tribological and electrical properties of Ag coating under current-carrying friction. *Friction* **9**(5): 978–989 (2021)

[30] Li S S, Chen H, Luo T, Xiao G C, Yi M D, Chen Z Q, Zhang J J, Xu C H. Tribological properties of laser surface texturing modified GCr15 steel under graphene/5CB lubrication. *J Mater Res Technol-*

JMRT **18**: 3598–3611 (2022)

[31] Gheisari R, Vazquez M, Tsigkis V, Erdemir A, Wooley K L, Polycarpou A A. Microencapsulated paraffin as a tribological additive for advanced polymeric coatings. *Friction* **11**(10): 1939–1952 (2023)

[32] Gulfam R, Orejon D, Choi C H, Zhang P. Phase-Change Slippery Liquid-Infused Porous Surfaces with Thermo-Responsive Wetting and Shedding States. *ACS Appl Mater Interfaces* **12**(30): 34306–34316 (2020)

[33] Jiang H, Chen X T, Fang Z Q, Xiong Y K, Wang H M, Tang X W, Ren J H, Tang P P, Li J P, Wang G Q, Li Z. NIR-Driven Self-Healing Phase-Change Solid Slippery Surface with Stability and Promising Antifouling and Anticorrosion Properties. *ACS Appl Mater Interfaces* **16**(26): 34089–34099 (2024)

[34] Xu C Y, Chen Z, Wang C X, Chen K L. Fabrication of Dual Self-Healing Multifunctional Coating Based on Multicompartment Microcapsules. *ACS Appl Mater Interfaces* **13**(49): 59298–59309 (2021)

[35] Zhang F, Ju P F, Pan M Q, Zhang D W, Huang Y, Li G L, Li X G. Self-healing mechanisms in smart protective coatings: A review. *Corrosion Sci* **144**: 74–88 (2018)

[36] Xue F, Yin T Q, Guo Z Y, Song J F, Ding Q J, Zhao G. Phase-Change Induced Capacitive Response in Lubricating Nanocapsules for In Situ Monitoring of Tribological Interface Temperature. *Adv Funct Mater*: e24480 (2026)

[37] Song X R, Hou Y Y, Zhang Y K, Ji X Y, Liu M M, Zheng H Y, Guo Z G. Multi-stimulus responsive anisotropic slippery surfaces. *Compos Pt B-Eng* **312**: 113322 (2026)

[38] Scaraggi M, Mezzapesa F P, Carbone G, Ancona A, Sorgente D, Lugarà P M. Minimize friction of lubricated laser-microtextured-surfaces by tuning microholes depth. *Tribol Int* **75**: 123–127 (2014)

[39] Schneider J, Braun D, Greiner C. Laser Textured Surfaces for Mixed Lubrication: Influence of Aspect Ratio, Textured Area and Dimple Arrangement. *Lubricants* **5**(3): 32 (2017)

[40] Lin J, Peng Z W, Liu Y Y, Ruiz-Zepeda F, Ye R Q, Samuel E L G, Yacaman M J, Yakobson B I, Tour J M. Laser-induced porous graphene films from commercial polymers. *Nat Commun* **5**(1): 5714 (2014)

[41] Ghosh S, Sahaluddin M, Abdulhafez M, Pwint M Y, Cui X T, Bedewy M. Miniaturizing Laser-Induced Graphene for Biosensors by Spatial Control of Initiation and Side-Selective Microfabrication on Commercial Polymers. *Accounts Chem Res*: e02433 (2025)

[42] Wang F C, Wang K D, Dong X, Mei X S, Zhai Z Y, Lv J, Duan W Q, Gao M. Tuning the Structures and Properties of Porous Graphene in Laser-Induced Graphitization. *J Laser Micro Nanoeng* **12**(2): 165–168 (2017)

[43] Ren Y L, Zhang L, Xie G X, Li Z B, Chen H, Gong H J, Xu W H, Guo D, Luo J B. A review on tribology of polymer composite coatings. *Friction* **9**(3): 429–470 (2021)

[44] Hua X J, Sun J G, Zhang P Y, Liu K, Wang R, Ji J H, Fu Y H. Tribological Properties of Laser Microtextured Surface Bonded With Composite Solid Lubricant at High Temperature. *J Tribol-Trans ASME* **138**(3): 031302 (2016)

Junhao Sang. He is a Master student from the School of Mechanical Engineering, Shandong University of Technology, Zibo, China, and a member of the Center for Advanced Laser Manufacturing. He focuses on the fabrication of laser micro/nano functional surfaces, the design of bioinspired lubricating interfaces, and research in the fields of friction reduction, wear resistance, and corrosion protection.

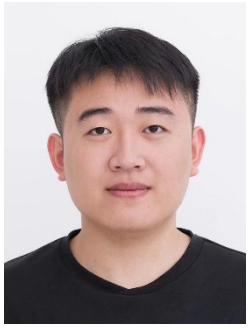

Yonglong Li. He is a doctoral student from the School of Mechanical Engineering, Shandong University of Technology, Zibo, China, and a member of the Center for Advanced Laser Manufacturing. He received the B.Mgt. degree in 2023 from the Southwest University. Chongqing, China. He focuses on the manufacturing of laser micro/nano functional surfaces, the design of flexible sensor devices, and research in the fields of triboelectric and piezoelectric nanogenerators. He has published 3 papers.

Xinyuan Ji. She is a Master student at the School of Mechanical Engineering, Shandong University of Technology (Zibo, China), and a member of the Center for Advanced Laser Manufacturing. Her focuses on the fabrication of oil-encapsulated microcapsule-filled polymer composite coatings to achieve synergistic protection against friction and corrosion. She has published 1 paper.

Yongling Wu. She received her B.Eng and M.Eng in Mechanical Engineering from Tsinghua University, China, and her Ph.D. in Materials Science and Engineering from Nanyang Technological University, Singapore, in 2009. She is currently a Professor at Shandong University of Technology, Zibo, China. She previously served as a Senior Scientist at the Agency for Science, Technology and Research (A*STAR), Singapore, and as the Group Manager of the Surface Technology Group. Her research areas include nanomaterials and coatings, surface science and engineering, functional materials and surfaces, and laser materials processing.

Mingming Liu. He received his Ph.D. degree from the Lanzhou Institute of Chemical Physics, Chinese Academy of Sciences in 2018. He current position is a Professor in Shandong University of Technology, Zibo, China. He has long been engaged in the basic research of multi-energy-field composite laser micro/nano manufacturing and surface engineering technology. He has published more than 70 SCI papers as the first author or corresponding author, including over 30 top papers in the JCR Q1 of the Chinese Academy of Sciences. It has been cited more than 2,000 times (H-30,Google Scholars).

Hongyu Zheng. He is the dean and distinguished professor in the School of Mechanical Engineering and director of the Centre for Advanced Laser Manufacturing (CALM) at Shandong University of Technology (SDUT), Zibo, China. He received his B.Eng in Mechanical Engineering from Tsinghua University, Beijing, China, in 1985, and his Ph.D. in laser materials processing from Imperial College London, London, UK, in 1990. Prior to joining SDUT, he was a principal scientist at the Agency for Science, Technology and Research (A*STAR) of Singapore. He is Fellow of the International Society of Nano-Manufacturing (ISNM), and has co-authored more than 300 scientific publications. His current research interests include ultrafast laser–matter interactions, two-photon polymerization, micro-/nano-processing mechanisms, in-process monitoring and data analytics.